IEEE Transactions on Haptics (ToH) paper, presented at ICRA 2026, Vienna, Austria. Cite as ToH paper.

Haptics of Pulse Palpation: Simulation and Validation through Novel Sensor-Actuator System

Debadutta Subudhi *IEEE Student,99564624* (Orcid Id-0000-0001-9801-4969), K. K. Deepak (0000-0003-0734-1097) and Manivannan Muniyandi (Orcid Id-0000-0003-1162-1550)

***Abstract*—Palpation of arteries holds significant physiological importance. Existing pulse actuator designs intended to replicate the haptic sensations of palpation primarily focus on normal force interactions, often overlooking the shear forces generated by oscillations of the arterial wall during blood flow. This study aims to evaluate the normal, longitudinal, and transverse forces exerted by arteries through both theoretical and experimental analyses during palpation. The experimental validation features a pulse actuator-sensor system. The actuator component is a hydro-electromagnetic actuator, while the haptic sensing is performed by the Subblescope. The Subblescope measures arterial force feedback from both soft and hard artery models, as well as from the radial pulse in 18 human subjects. Mathematical analysis establishes the operational range of the sensor-actuator system as $0.005\,\mathrm{N}$ to $2.5\,\mathrm{N}$. The force feedback from the simulation has been used for designing the total force generation by the actuator. The reactive force along the Z-axis varies between $19.3\,\mathrm{mN}$ to $500\,\mathrm{mN}$, while the transverse and longitudinal forces along the Y and X axes range from $6.9\,\mathrm{mN}$ to $88.01\,\mathrm{mN}$ and $5.46\,\mathrm{mN}$ to $87.85\,\mathrm{mN}$, respectively. The pulse-force map of the hard artery reveals higher three-dimensional force interactions compared to the soft artery. The hydroelectromagnetic actuator effectively generates both normal and shear forces during pulsatile flow. Future work will focus on developing training modules that replicate pulse haptics associated with various physiological conditions, such as diabetes.**

***Index Terms*—Pulse palpation, pulse force, Subblescope, Hydro-electromagnetic actuator, Robotic indentation, UR3e.**

I. Introduction

PULSE palpation is a tactile examination technique that involves the use of fingers through both prehensile (grasping) and non-prehensile (pushing) movements [1]. It enables physicians to assess cardiovascular dynamics by evaluating pulse rate, variability, amplitude, and width [2]. Beyond these metrics, haptic cues, such as force feedback from the artery and oscillations of the arterial wall, also hold physiological significance during palpation. Palpation may involve one or more fingertips, depending on the clinical context. Physicians often examine multiple anatomical sites and arteries—including the carotid, radial, brachial, and femoral—to assess the patient's condition [3]. Changes in the aforementioned pulse parameters are influenced by several physiological factors, including blood composition, ventricular contraction, valve function, and vascular stiffness.

Pulse assessment techniques can be broadly categorized into contact and non-contact methods. Non-contact methods are typically based on optical or radar sensing principles, which primarily capture one-dimensional characteristics of the pulse. Optical sensing techniques include photoplethysmography [4], fiber Bragg grating sensors [5], and binocular vision tracking of marker displacement on a deformable diaphragm [6]. Radar-based systems utilize radio frequencies to measure the temporal phase difference between transmitted and received signals from the body surface, particularly the arm [7]. In contrast, pulse assessment through isometric contraction of the artery during palpation provides a different approach. It allows for the detection of localized flow variations. As blood flows through a converging-diverging arterial segment—modeled as an elliptical channel. This mechanical deformation of the artery during palpation may enable the generation of spatial force maps, offering a more detailed physiological representation of the arterial pulse.

Recent efforts in arterial palpation training during surgery have utilized virtual reality (VR) and augmented reality (AR) platforms, where various pulse types are simulated on manikins [8], [9]. However, accurately replicating pulse variation through palpation in VR and AR environments requires a clear understanding of force magnitude, distribution, and actuation mechanisms. One such system, PalpSim, integrates palpation physics into a VR setup using two Falcon force-feedback devices connected by a silicone tray housing tactile actuators. This configuration simulates the palpation of the femoral artery [10]. In PalpSim, increased actuator displacement corresponds to a stronger pulse sensation, and vice versa.

The wearable Hap-Pulse glove employs three linear resonant actuators (LRAs) with a natural frequency of $175\,\mathrm{Hz}$ to simulate four pulse types, differentiated by pulse width in ms [11]. Although the glove produces a unidirectional, modulated pulse waveform that allows users to perceive both the signal envelope and vibration, its feedback is limited to a single direction. Existing pulse simulators mainly employ single-point tactile actuators based on piezoelectric, capacitive, pneumatic, or electromagnetic principles. These devices typically deliver only unidirectional force feedback, overlooking the tangential forces generated by longitudinal arterial wall motion (LWM)—a known independent predictor of cardiovascular morbidity [12]. Additionally, transverse wall oscillations (TOs), which may correlate with pulse wave velocity (PWV), are influenced by arterial stiffness and provide further diagnostic value [13]. High-fidelity replication of pulse palpation requires fluid-based actuators capable of delivering multi-directional force interactions at the palpation site. These actuators incorporate both longitudinal wall motion (LWM) and transverse oscillations (TOs) into the

D. Subudhi and Manivannan M. are with the Touch Lab, Center for Virtual Reality and Haptics, Indian Institute of Technology Madras, India, 600036 (e-mail: dev.subudhi49@gmail.com, mani@iitm.ac.in). K K Deepak is with Center of Biomedical Engineering, Indian Institute of Technology Delhi, New Delhi, Delhi, 110016, India

IEEE Transactions on Haptics (ToH) paper, presented at ICRA 2026, Vienna, Austria. Cite as ToH paper.

haptic feedback system to accurately simulate physiological conditions. During arterial palpation, the fingertips perceive both force and motion, making it essential to consider the perceptual thresholds of these stimuli.

This study focuses on the force perception threshold, as the sensor employed is calibrated to measure forces resulting from deformation fields under both normal and shear loading. The Weber fraction for force perception ranges from 10% to 45% for reference forces between $1.5\,\mathrm{N}$ to $3.5\,\mathrm{N}$, across both passive and active interactions at the index finger, thumb, and upper arm regions [14]. As such, the haptics of pulse palpation involves three-dimensional force input from arterial pressure and wall motion in response to finger-induced deformation—an aspect that remains underexplored in the current body of literature.

1) Force perceptual threshold: The physical stimulus space comprises haptic parameters encompassing both kinematics and kinetics. Mapping these parameters into perceptual space is quantified by the absolute threshold and the Weber fraction, also known as the Just Noticeable Difference (JND) [14]. Among these measures, the force perception threshold (FPT) is critical for designing sensor-actuator systems in pulse haptics. One study measures the force threshold using a two-interval force choice (2IFC) method, applying force via Weinstein nylon filaments ranging from $0.0045\,\mathrm{g}$ to $447\,\mathrm{g}$ ($0.04\,\mathrm{mN}$ to $4.3\,\mathrm{mN}$). The absolute threshold is found to be $0.14\,\mathrm{mN}$ for young participants and $0.6\,\mathrm{mN}$ for older participants [15], with a detection probability of 0.5 attributed to the manual application of the filaments. The relevant pulse frequency band lies between $0.5\,\mathrm{Hz}$ to $10\,\mathrm{Hz}$ [16], within which the absolute force threshold for the index finger is approximately $19\,\mathrm{mN}$ [14]. Spatial summation effects reduce the force perception threshold to $28.9\,\mathrm{mN}$ when force feedback is delivered through a multi-finger haptic device (MFHD). However, the absolute thresholds for individual fingers vary, with the index, middle, pinkie, and ring fingers registering thresholds of $33.5\,\mathrm{mN}$, $32.1\,\mathrm{mN}$, $33.5\,\mathrm{mN}$, and $43.6\,\mathrm{mN}$, respectively. Collectively, the literature indicates that force inputs exceeding approximately $19\,\mathrm{mN}$ are generally perceivable by the fingertips.

II. Related works

The fundamental method for generating an arterial pulse involves the reciprocation of a diaphragm. The diaphragm's movement is controlled by various actuation mechanisms, detailed as follows:

- **Electromagnetic:** A solenoid activated by electric current generates an electromagnetic field that interacts with nearby magnetic fields, producing a Lorentz force that displaces the plunger perpendicular to the magnetic field [17].
- **Electrostatic:** The Coulomb attraction force between oppositely charged parallel plates subjected to kilovolt-range voltages is expressed as $F = \frac{\epsilon_0 \epsilon_r A V^2}{2x^2}$, where A is the electrode area, V the applied voltage, and x the electrode separation [18], [19].
- **Voicecoil:** An electric current supplied to the coil generates sound waves that interact with the diaphragm to produce the desired tactile pulse characteristics [20].
- **Linear Resonant Actuators (LRAs):** LRAs operating at a resonant frequency of $175\,\mathrm{Hz}$ generate pulse-modulated waveforms with diverse morphologies, varying widths, and pulse rates [11].
- **Piezoelectric:** Application of an electric field to a piezoelectric disk attached to the diaphragm produces actuation forces with rapid response times [21].
- **Pneumatic:** Compressed air directed through valves inflates the diaphragm, delivering tactile feedback to the fingertips [22].
- **Thermopneumatic and Shape Memory Alloy (SMA):** Internal heaters transfer energy to air, causing expansion and diaphragm deformation to generate pulses [23]. SMA heating induces alternating diaphragm deformation to produce pulsatile effects [24].
- **Magnetohydrodynamic:** Conductive or magnetorheological fluids are actuated by orthogonal magnetic and electric fields to simulate pulses [25], [26].
- **Hydraulics:** Stepper motors actuate pistons within fluid-filled chambers, generating pulses in silicone artery phantoms [27], [28].
- **Cam System:** A triple cam mechanism, driven by three stepper motors operating with phase differences, modulates compressed air to replicate forward, first reflected, and second reflected arterial waves corresponding to different age groups [29].
- **PHANTOM Omni:** The Phantom Omni device produces pulse forces ranging from $0\,\mathrm{N}$ to $1.0\,\mathrm{N}$ at 40–160 beats per minute, with the end effector positioned within a manikin hand [30].
- **Mock Circulatory Loop (MCL):** The MCL, used for cardiac assistance and vascular disorder testing, generates pulses in silicone elastomer phantoms via pneumatic ventricular chamber actuation [31], [32], spring-coupled piston-cylinder systems [33]–[35], pulsatile pumps [36], and compliance chambers filled with air and circulating fluid [35].

Despite the variety of existing methods, electromagnetic actuation remains the predominant approach for generating human-like pulses, primarily due to its compactness and ease of integration within manikins. Most mock circulatory simulators maintain ventricular compliance by regulating air pressure. However, pneumatic actuators described in the literature often fail to replicate pulse dynamics analogous to blood flow, largely due to differences in fluid viscosity. Cam-based simulators require multiple cam profiles to reproduce the full spectrum of pulse-wave morphologies. Furthermore, the majority of actuators focus on force and displacement along the vertical axis, despite blood pressure exerting forces in transverse and longitudinal directions as well.

Consequently, haptic interaction with an artery involves forces along radial, transverse, and longitudinal axes. This necessitates a haptic sensor capable of measuring pulse forces in all three directions, alongside a pulse actuator to validate these forces during palpation. To address this, we have developed a sensor-actuator system designed to evaluate force interactions during arterial palpation. The sensor measures forces in three

IEEE Transactions on Haptics (ToH) paper, presented at ICRA 2026, Vienna, Austria. Cite as ToH paper.

directions, while the hydro-electromagnetic actuator (HEMA), inspired by designs from mock circulatory loops, generates pulsatile forces for validation. The sensor-actuator system for pulse recording and generation is well documented in the literature. However, the fundamental haptics of pulse palpation and the quantification of palpation metrics remain insufficiently explored. Most studies focus primarily on normal force feedback, which depends largely on arterial elasticity. In contrast, shear forces are influenced by blood viscosity, which varies with blood constituents and flow characteristics—parameters critical to physiological function. Arterial wall oscillations reflect the fluid–structure interaction; longitudinal wall motion correlates with pulse wave velocity (PWV), while transverse wall oscillations relate to vascular compliance.

This paper presents a conceptual framework, supported by simulations and experiments, utilizing an in-house sensor-actuator system to elucidate the fundamental pulse dynamics during single-finger palpation. The study quantifies force feedback along the X, Y, and Z axes in response to applied forces or fixed indentations on the artery.

III. Methods

This study investigates the effect of single-finger palpation on various types of arteries. Force interactions along the X, Y, and Z axes are examined for a fixed indentation of $1.0\,\mathrm{mm}$ applied to arteries representing different vascular properties, including soft and hard types. To facilitate intuitive understanding, a two-dimensional mathematical model of single-point palpation is introduced to characterize the magnitude of reactive forces during palpation of flexible and stiff arteries. Both simulation and experimental methods are employed to analyze three-dimensional force interactions during palpation on soft and hard arteries.

The tube law [37] is applied to estimate pressure distribution within the palpated region, serving as a surrogate measure for pulse wave velocity (PWV). Simulations use the arbitrary Lagrangian-Eulerian (ALE) approach in COMSOL Multiphysics 6.1 to capture fully coupled fluid-structure interactions (FSI) [38]. The simulated force interactions inform the actuator design by determining the total force required to sustain circulation. Experimentally, a sensor-equipped apparatus records the spatiotemporal force of the pulse. An in-house developed hydro-electromagnetic actuator generates pulses within a silicone artery to validate the sensor's performance. Finally, the sensor measures force directly from the radial artery of human subjects, reflecting real physiological conditions.

A. Theoretical Analysis

1) Mathematical Background to Artery Palpation: The palpation has a Gaussian-distributed force pattern, and the flow inside the artery follows through a curved arterial segment. The pressure difference along the curvature of the artery is governed by the tube law [37]. The pressure difference at the artery interface is due to blood flow (dP_v) and pulse wave velocity (dP_{pwv}) given by 1 and 2, respectively. The resultant pressure change along the interface is given by equation 3.

$$dP_{\text{pwv}} = dp_e + \rho_a c^2 \frac{d\alpha}{\alpha} + K_p \frac{\partial P_f}{\partial x}\, dx + P_f\, dK_p \tag{1}$$

$$dP_v = \rho_b U^2 \frac{dA}{A} - \frac{\mu_b U f_L dx}{d^2} \tag{2}$$

$$dP = dP_{\text{pwv}} + dP_v \tag{3}$$

Where c is the pulse wave velocity in m/sec given as $c = \sqrt{n\,(\alpha^{-n})\,\frac{K_p}{\rho_b}}, n = \frac{3}{2}$ [37]. $K_p = \frac{F_p}{\delta}$, δ is deflection of artery segment due to palpation, F_p is the palpation force $\alpha = \frac{delta}{d_i}$ is the radial strain, d_i is the initial diameter of the artery. The ρ_a $=1160\,\mathrm{kg\,m^3}$, ρ_b $=1050\,\mathrm{kg\,m^3}$ is the density of the artery wall and blood respectively [39], $\mu_b = \mu_0 * \epsilon_r^{m-1}, m = 0.5$ is the viscosity of blood as a function of radial strain rate ($\epsilon_r = \log(1+\alpha)$) due shear thinning behavior ($m < 1$) [40]. The flow is laminar. Since the maximum Reynold's number is 602.6, therefore the friction factor f_L is given by $f_L = \frac{16}{Re}$. The artery wall is assumed to be uniformly supported by the mean arterial blood pressure (MAP), which is $93.33\,\mathrm{mmHg}$ for a standard systolic and diastolic pressure of $120\,\mathrm{mmHg}$ and $80\,\mathrm{mmHg}$, respectively. The mathematical representation of artery loading through palpation is shown in Figure 1a. The boundary effect lies between $0\,\mathrm{mm}$ to $0.105\,\mathrm{mm}$ and $17.9\,\mathrm{mm}$ to $18\,\mathrm{mm}$; hence is not considered for the analysis. The width of the artery is assumed to be unit, with thickness (t $=0.42\,\mathrm{mm}$ [41] and modulus of elasticity is $0.505\,\mathrm{MPa}$, $0.93\,\mathrm{MPa}$ for soft and hard arteries [42]. The mean diameter of the radial artery is $2.79\,\mathrm{mm}$ [41]. The length of the palpated artery segment is $l_a = 18\,\mathrm{mm}$ equivalent to the average width of a human finger [43]. The palpation force has a Gaussian distribution. Its magnitude has been modified for both soft ($F_{\text{artery}} = 8.5e-5N$) and hard ($F_{\text{artery}} = 17.8e-5N$) arteries so as to have equal deformation given by equation 4, and the effective reaction force at 'A' is given by expression 5.

$$F_p = \frac{F_{\text{artery}}}{\sqrt{2\pi}\times 2} \exp\left(-\frac{1}{2}\left(\frac{x-8}{2}\right)^2\right) \tag{4}$$

$$R_A = \frac{\int_0^{l_a} F_p\, dx}{2} - \frac{p_{\text{map}} \times A_c}{2} \tag{5}$$

The moment at any cross-section X-X at a distance x from 'A' is given by 6.

$$M_x = R_A \times x - \left(\int_0^{l_a} F_p\, dx\right) \times (x - x_c) x_c = \frac{\int_0^{l_a} F_p \cdot x\, dx}{\int_0^{l_a} F_p\, dx} \tag{6}$$

The deflection of the artery wall is obtained using equation 7.

$$EI\frac{d^2y}{dx^2} = M_x \tag{7}$$

The boundary conditions are the Neumann condition at $x = l_a/2$,i.e $\frac{dy}{dx} = 0$, and the Dirichlet condition at $x = 0$ where $y = 0$ to obtain the integrating constants. The analytical method estimates the overall range of force interaction during arterial palpation along the vertical axis. Forces along the transverse and longitudinal directions are evaluated through simulation. The resultant force obtained from the simulation

IEEE Transactions on Haptics (ToH) paper, presented at ICRA 2026, Vienna, Austria. Cite as ToH paper.

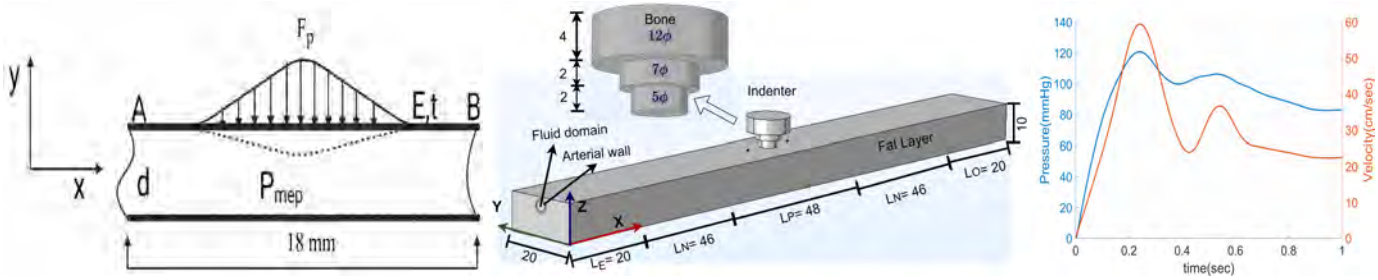

(a) Artery Loading (b) Simulation setup (c) Boundary condition

Fig. 1: **a**.Mathematical representation of palpation on the artery in 2D **b.** Simulation setup of three-dimensional artery model including fluid as blood, solid domains constitute the arterial wall, fat layer, and a single indenter. The dimensions are in mm.**c**. Velocity (orange) and pressure (blue) boundary conditions at inlet and outlet, respectively.

is used to determine the maximum force the actuator must generate to maintain pulsatile flow during palpation along with inertia and compression forces.

2) Simulation setup: The FEA simulation analyses stress distribution along the length and top surface of the artery during single-finger palpation through FSI.

Geometry: The artery has a neck length (L_N) of $46\,\mathrm{mm}$ [44] with a palpable length of $48\,\mathrm{mm}$ single indenter as shown in Fig. 1b. The palpable length varies depending on finger placement. The entry (L_E) and exit length (L_O) are $20\,\mathrm{mm}$ each to obtain a fully developed flow by reducing the boundary effect. Therefore, the overall length of the artery is $180\,\mathrm{mm}$. The diameter and thickness of the artery are described in III-A1. The indenter has a stepped cylindrical structure, as shown in Fig. 1b.

Fluid Model: The fully coupled FSI of blood flow with the palpated artery uses the arbitrary Lagrangian-Eulerian (ALE) approach, thereby allowing the fluid mesh to update as per the artery wall motion. The continuity and momentum equations for the fluid are given by equations 8 and 9.

$$\nabla.U = 0 \tag{8}$$

$$\rho(\frac{\partial U}{\partial t} + (U^r.\nabla)U) = \nabla p + \nabla \tau_f \tag{9}$$

Where ρ is the density of blood. U is the fluid velocity, and U^r is the relative velocity of a fluid with respect to moving reference velocity. Blood is assumed to be homogeneous, incompressible, and Newtonian fluid. This assumption is acceptable for vessel diameter exceeding $0.5\,\mathrm{mm}$ [45]. The dynamic viscosity of blood at 37^0C is $0.0045\,\mathrm{Pa\,s}$ [46]. The flow is laminar.

Structure Model: The hemodynamic forces cause displacement in the arterial wall in response to the indentation. The displacement is captured by the Lagrangian coordinate system on the solid domain through the following equations 10, 11.

$$\nabla.\sigma_{ij} = \rho_a * \frac{\partial^2 u_{solid}}{\partial t^2} \tag{10}$$

$$\sigma_{ij} = E\epsilon_{kl} \tag{11}$$

Where σ_{ij} is the solid stress tensor, E is the modulus of elasticity of the artery wall, ϵ_λ is the solid strain tensor, and ρ_a is the artery wall density ($1160\,\mathrm{kg\,m^{-3}}$ [47]). The two domains are coupled through compatibility and traction conditions [46]. The artery wall, fat domain, and fingertip have been modeled as a hyperelastic material constraint with Yeoh parameters as $C_1 = 0.084163\mathrm{MPa}, C_2 = -0.15575\mathrm{MPa}, C_3 = 0.1924$ MPa respectively for the soft vasculature made up of Ecoflex 00-31 as shown in Fig. 2e. The true stress and stretch are related by the following expression 12

$$\sigma_t = (\lambda - \frac{1}{\lambda^2})(2 * C_1 + 4 * C_2 \left(\lambda^2 + \frac{2}{\lambda} - 3\right) + 6 * C_3 \left(\lambda^2 + \frac{2}{\lambda} - 3\right)^2) \tag{12}$$

The modulus of elasticity for small deformation during pulsatile flow is given by equation 13 [48].

$$E = \frac{d\sigma_t}{d\lambda} = 0.505MPa \tag{13}$$

The Yeoh material constants for the hard artery is $C_1 = 0.15416\mathrm{MPa}, C_2 = -0.45575\mathrm{MPa}, C_3 = 0.5924$ MPa respectively, which results in modulus of elasticity of $0.92\,\mathrm{MPa}$.

The fingertip has a tri-cylindrical stepped structure equivalent to the skin layer, constituting the dermis, hypodermis, and bone layer. The dermis layer has a diameter of $5\,\mathrm{mm}$ and height of $2\,\mathrm{mm}$. The hypodermis layer has a diameter of $7\,\mathrm{mm}$ and height of $2\,\mathrm{mm}$. The bone layer has a diameter of $12\,\mathrm{mm}$ and height of $2\,\mathrm{mm}$. The dermis and hypodermis have material similar to that of the fat domain. The bone layer has a linearly elastic property with a density of $2000\,\mathrm{kg\,m^{-3}}$ Young's modulus of $17.5\,\mathrm{GPa}$, and a Poisson ratio of 0.3 [49].

Boundary Conditions: The inlet boundary condition for the pulsatile flow is a time-dependent velocity, and the outlet boundary condition is a time-dependent pressure, as shown in Fig. 1c [46].

Assumptions in the model:

1) Fluid velocity at the tube walls is equal to the wall velocity as the tube walls are not rigid.
2) The blood is a Newtonian fluid and incompressible
3) The artery walls and the indenter tip are homogeneous, and the mechanical properties are the same as that of the fat layer surrounding the artery to reduce the complexity of varied mechanical properties for each layer.

IEEE Transactions on Haptics (ToH) paper, presented at ICRA 2026, Vienna, Austria. Cite as ToH paper.

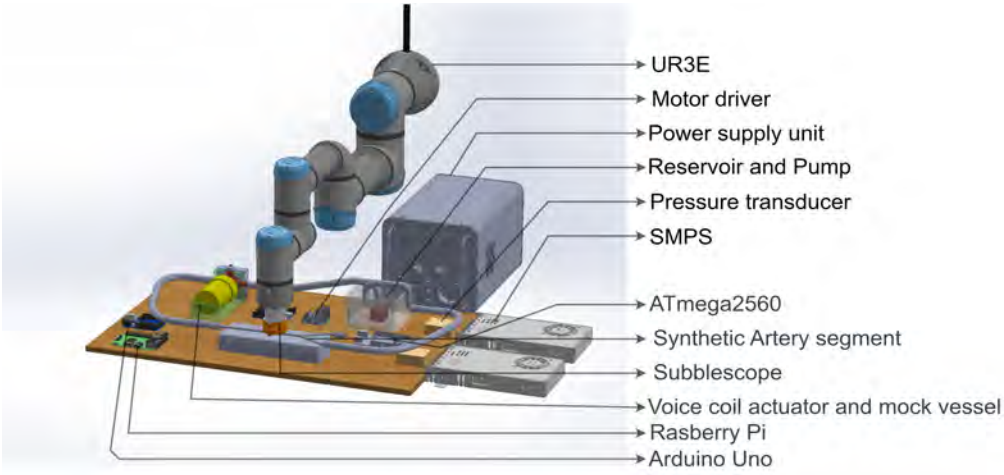

(a) Hydro-electromagnetic actuator

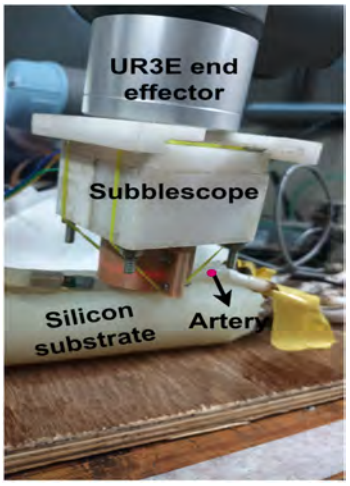

(b) Palpation

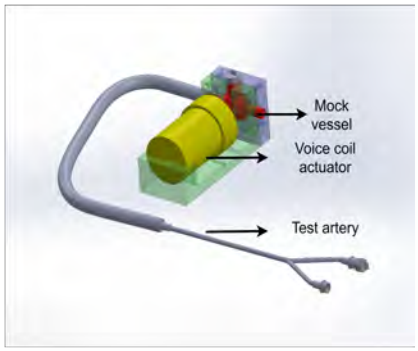

(c) Mock vessel

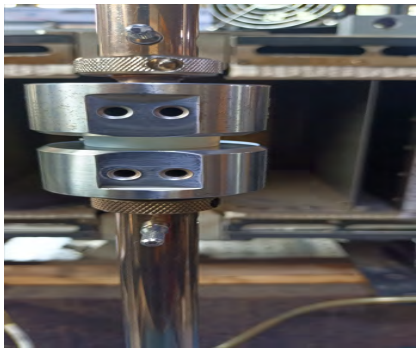

(d) Compression Test

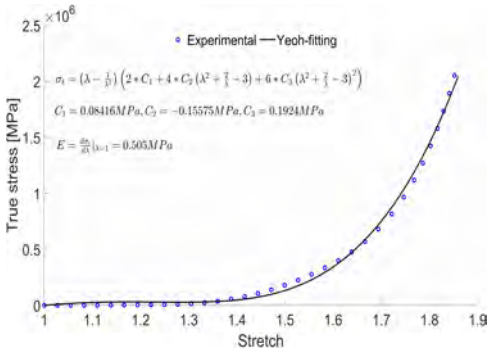

(e) Yeoh fitting

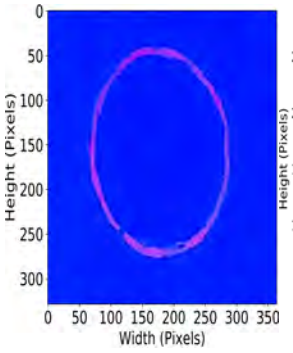

(f) Initial configuration

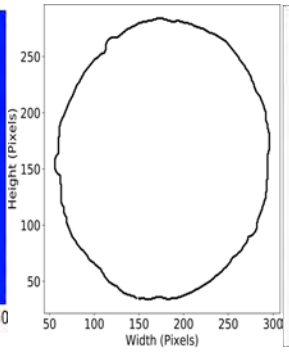

(g) Large Contour

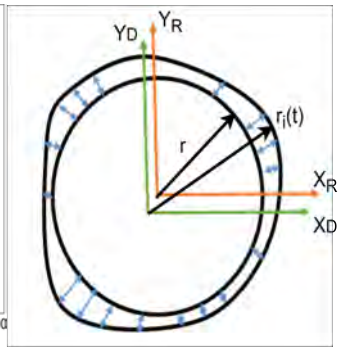

(h) Contour displacement

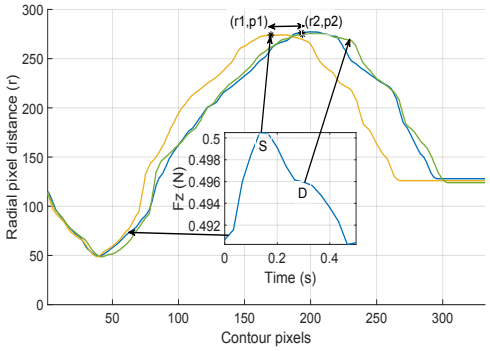

(i) Radial Displacement

Fig. 2: **a**.Schematic representation of experimental set-up for generating the pulse and recording the pressure waveform from the single ventricle chamber, the end of the arterial branch, and force from the test artery segment while palpated by the Subblescope attached to the UR3E **b**. Replication of palpation by UR3E on the Synthetic artery made up of silicon rubber of Ecoflex 00-31 placed onto the silicon substrate. The artery and the substrate are manufactured by the molding process. **c.** The mock vessel is encapsulated between the PLA enclosure and is actuated externally by the voice coil actuator. **d.** Compression test of artery-making material made up of Ecoflex $00-31$ silicon rubber specimen as per ASTM IV in micro-UTM at a rate of $6\,\mathrm{mm\,min^{-1}}$. **e.** Stress-stretch curve and hyperelastic model (Yeoh) fitting to the experimental data, showing the modulus of the material as $0.505\,\mathrm{MPa}$.**f.** The initial configuration of the bubble in the elastomer. **g.** The large contour in the bubble. **h.** Graphical presentation of centroid movement and change in perimeter of the bubble. **i.** The linear displacement of the perimeter.

4) The bone layer atop the indenter is linearly elastic.
5) Except for the bone layer, all the model parts are assumed to be hyperelastic to behave like tissue material, with the same elastic constants as obtained experimentally.
6) The body force is neglected, and only the effect of external force during palpation onto the artery walls is considered.
7) The roller boundary conditions are applied on all the surfaces except the top and side surface of the fat layer
8) The solid domain is isotropic and homogeneous

Model Implementation: We employ COMSOL 6.1 as

IEEE Transactions on Haptics (ToH) paper, presented at ICRA 2026, Vienna, Austria. Cite as ToH paper.

a finite element solver to address the fully coupled fluid-structure interaction on a desktop PC equipped with an Intel Core i7-7700 CPU, 32.0 GB of RAM, and Microsoft Windows 11 64-bit. The automatic Newton method utilizes a PARDISO solver with a relative tolerance of 0.001. The mesh is user-regulated with free tetrahedral elements, featuring extra-fine meshing for the fluid, artery wall, and dermis, while the other domains exhibit finer meshing [50]. Boundary layers are implemented in the fluid domain and its boundaries, utilizing two layers and a stretching factor of 1.2. The comprehensive mesh has 189,378 domain elements, 27,171 boundary elements, and 2,804 edge elements. The FSI employs the time-dependent blood flow solution as the independent variable and the arterial deformation resulting from indentation as the dependent variable in the multiphysics coupling. The artery has been compressed by the stationary movement of the indenter in the z-direction by $1\,\mathrm{mm}$. The time-dependent solver utilizes an implicit backward differentiation formula (BDF) or the backward Euler method for solving partial differential equations.

B. Experiment setup

The experimental setup consists of measuring pulse dynamics using Subblescope [51] on the pulse actuator system and radial artery of 18 participants as approved by the Institutional Ethical Committee (IEC) of IIT Madras, with the reference number $(IEC/2023-03/MM/02/03)$.

1) 3D Pulse-force assessment by Subblescope: The Subblescope measures both normal and shear forces through the deformation of a bubble embedded within an elastomer. A vision system captures the bubble's deformation, which has been calibrated against known normal and shear forces [51]. A pure normal force causes uniform expansion or contraction of the bubble's perimeter or radius, with the bubble's centroid remaining fixed. In contrast, an applied shear force at the indenter induces a shear and bending moment at the indenter's base, resulting in an asymmetric deformation of the bubble. This deformation shifts both the centroid and the contour of the bubble, causing the radius to vary unevenly along its periphery, as illustrated in Figure 3a.

Algorithm: The algorithm estimates the normal, radial, and tangential forces by calibrating bubble deformation against known normal and shear forces applied using a Microtensile Universal Testing Machine (Instron-5948) on the sensor [51]. The original, undeformed bubble perimeter is shown in Fig. 2f, with its contour depicted in Fig. 2g. The force determination procedure is detailed in Algorithm 1, accompanied by a graphical representation in Figs. 2h and 3a. Additionally, Fig. 2i illustrates the radial displacement of the bubble during the initial phase, systole, and diastole of a pulsatile artery. The bubble area correlates with the normal force, while the maximum radial displacement and its location, calibrated through shear force measurements, correspond to the radial and tangential forces, respectively.

Algorithm 1 Normal and shear forces from the bubble deformation

WHILE($\mathbf{i} < \mathbf{FrameLength}$)
Converting to Gray image
Contrast enhancing by CLAHE
Thresholding between 120 to 255
Closing operation to fill discontinuity
Gaussian blurring
Edge detection by Sobel gradient
Contour detection
$A_c \leftarrow area(contour)$
$d_x \leftarrow x_c$,
$d_y \leftarrow y_c$,
$d_c \leftarrow \sqrt{(Contour_x - x_c)^2 + (Contour_y - y_c)^2}$,
$[peak, loc] \leftarrow max(d_c)$
$F_z \leftarrow f(A_c) \leftarrow 1.364e-9 * A_c^2 - 0.000108 * A_c + 2.02$
$F_y \leftarrow f(r_{max}) \leftarrow 0.007031 * r_{max} - 2.25$
$F_x \leftarrow f(r_{loc}) \leftarrow -0.001037 * r_{loc} + 0.287$

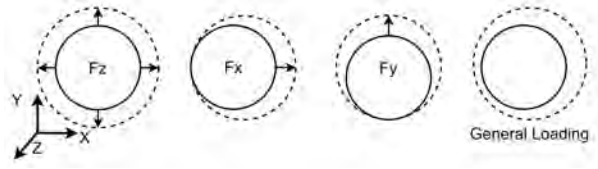

(a) Peripheral deformation

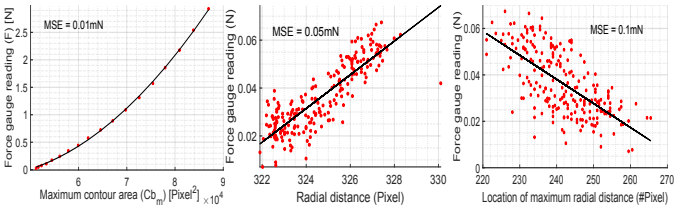

(b) Normal force (c) Radial force (d) Tangential force

Fig. 3: **a.** Peripheral movement of the bubble by normal, shear and generalized loading conditions. Calibration curve for the **b.** normal, **c.** radial, and **d.** tangential loading.

2) Hydro-electromagnetic pulse actuator: The pulse simulator comprises five primary components: the mock vessel (ventricle), voice coil actuator, arterial branch, artery substrate, hydraulic circuit for high-fidelity pulse generation, and a robotic arm equipped with a sensor for artery palpation.

The mock vessel is fabricated from silicone rubber with a hardness of 25 A. The volume of the single chamber-ventricle is $50\,\mathrm{mL}$. The mock vessel is housed within a fixture that contains the voice coil, as illustrated in Fig. 2c. A motor driver with a microcontroller (Arduino Uno) actuates the voice coil to have different stroke lengths and forces. The power supply unit delivers $12\,\mathrm{V}$ DC and a peak current of $0.32\,\mathrm{A}$ while powering the voice coil. The stroke length is $6.0\,\mathrm{mm}$, configured to produce several pulse forms of differing magnitudes. The experimental configuration has been evaluated using a sinusoidal pulse at 1.8 Hz as the input. The hydraulic circuit

IEEE Transactions on Haptics (ToH) paper, presented at ICRA 2026, Vienna, Austria. Cite as ToH paper.

consists of two one-way valves positioned at the inlet and outlet of the mock vessel, a reservoir, and a submersible pump with a power rating of $5\,\mathrm{W}$ and a flow rate of $300\,\mathrm{L\,h^{-1}}$, which corresponds to the typical cardiac blood flow rate. The test artery segment measures $140\,\mathrm{mm}$ in length, excluding the branched artery, possesses a thickness of $1\,\mathrm{mm}$, which falls within the human arterial thickness range of $0.45\,\mathrm{mm}$ to $1.25\,\mathrm{mm}$ [52], and has a diameter of $2.5\,\mathrm{mm}$, which falls within the range of $1.26\,\mathrm{mm}$ to $3.48\,\mathrm{mm}$ [52]. The material consists of Ecoflex $00-31$ silicon rubber, molded to achieve a modulus of elasticity of $0.505\,\mathrm{MPa}$ under compression, as depicted in Fig. 2e, which corresponds to the elastic modulus of an artery, typically rkhamdaeng2012arterial. The modulus of elasticity was experimentally determined during a uniaxial compression test using the MicroUTM (Instron 5948), as seen in Fig. 2d. The rigid artery is composed of 20A silicone rubber. The artery is situated beneath the flexible substrate composed of Ecoflex 00-31, which is imprinted with the dimensions of the radius and ulnar bones corresponding to the human hand. The pressure transducers are located in the ventricular chamber and at the terminus of the arterial branch to gauge the pressure. The artery is palpated using the in-house designed force sensor, Subblescope [51], to measure the force interaction from the artery during palpation, as seen in Fig. 2a. The Subblescope is affixed to the end effector of a UR3e robotic arm to exert a consistent indentation of $1\,\mathrm{mm}$ on the artificial silicon artery and the human radial artery to capture the tactile characteristics of the pulse.

The experiment investigates artery wall motion generated by the actuator, recorded through bubble deformation in the Subblescope. Distortion of the bubble's boundary and centroid during pulsatile flow leads to spatial displacement of the pulse, as shown in Fig. 2h. The actuator design is governed by the magnitudes of several force components: the compression force applied to the chamber (F_c), fluid pressure force (F_p), inertial force from moving components (F_i), and the resultant force interaction during palpation (F_{palp}). The total force required for effective pulse generation is expressed as: $F_{tot} = F_c + F_p + F_i + F_{palp}$. The mock vessel is constrained along its periphery by a PLA enclosure, except at the front, where a circular opening of diameter $D = 20\,\mathrm{mm}$ allows plunger access. Controlled motion of the plunger through this opening compresses the vessel, thereby displacing the diaphragm to produce a pulsatile flow. The plunger is fitted with a cylindrical PLA plate of diameter $d = 10\,\mathrm{mm}$ and operates with a stroke length of $5.0\,\mathrm{mm}$. As a result, the diaphragm undergoes a deformation of $w = 5.0\,\mathrm{mm}$. The force required to produce this deformation, F_c, is calculated using Eq. 14.

$$w = \frac{F_c}{8\pi Z}\left[\frac{D^2-d^2}{4}\left(1+\left(\frac{1}{2}\cdot\frac{1-\nu}{1+\nu}\cdot\frac{D^2-d^2}{d^2}\right)\right) + \frac{d^2}{2}\log\left(\frac{D}{d}\right)\right] \tag{14}$$

where Z is the flexural rigidity of the diaphragm given by $Z = \frac{Eh^3}{12(1-\nu^2)}$, $\nu = 0.49$ is the Poisson ratio of the diaphragm. 'h=$3.0\,\mathrm{mm}$' and 'E = $0.92\,\mathrm{MPa}$' are the thickness and modulus of elasticity of the vessel's wall. The force required to move the diaphragm by $5.0\,\mathrm{mm}$ is $2.7\,\mathrm{N}$ as per equation 14. The water is circulated by the $5.0\,\mathrm{W}$ submersible pump with a flow rate of $5\,\mathrm{L\,min^{-1}}$ or $8.33\times10^{-5}\ \mathrm{m^3\,s^{-1}}$, considering a pump efficiency of 60%, the pressure difference is $\frac{5\cdot0.6}{8.33\times10^{-5}} = \frac{3}{8.33\times10^{-5}} \approx 36\,000\,\mathrm{Pa}$. Therefore, the force from the fluid pressure onto the diaphragm is $2.82\,\mathrm{N}$.
The inertial force from the moving parts is $F_{int} = m.a_{max}$, m is the mass of the moving parts as $1.1\,\mathrm{kg}$ and the maximum acceleration (a_{max}) is $w * \omega^2$. The frequency of the pulse can go to a maximum of $3.3\,\mathrm{Hz}$ [53] considering the fibrillation condition. Therefore, the inertial force becomes $F_{int} = m.a_{max} = 1.1 * (2\pi * 3.3)^2 * 0.005 = 2.36\,\mathrm{N}$.
The F_{palp} needs to be calculated from the simulation while indenting the artery by $1.0\,\mathrm{mm}$. The viscous force can be neglected compared to the inertia and hydrodynamic forces. Hence, the total force is the sum of all these forces, which turns out to be $7.88\,\mathrm{N}$ except the F_{palp}. Hence, the voice coil selection is based on the stroke length of $5.0\,\mathrm{mm}$ and twice the calculated force of $7.88\,\mathrm{N}$ for pulse actuation. The CVC 40-HF-6.5 satisfies these specifications with a stroke length of $6.5\,\mathrm{mm}$ and continuous force rating of $45.5\,\mathrm{N}$.

3) Measurement from the real arteries: The structural complexity of the artery and its surrounding connective tissues results in equally complex force interactions during palpation. To capture these interactions, this study includes force measurements from the radial artery of eighteen human participants (aged 30 ± 6 years). The Subblescope sensor is mounted on the end effector of a robotic arm, which applies a fixed skin indentation of $3\,\mathrm{mm}$ to access the artery. Pulse signals are recorded continuously for $60\,\mathrm{s}$ for each participant.

IV. Results

The results analyze the force range at the top surface of the indenter tip during palpation evaluated through analytical and experimental approaches.

A. Force interaction from mathematical model

The mathematical model delineates the extent of the deflection profile of the artery in relation to the Gaussian load. The deflection of both soft and hard arteries is standardized by adjusting the peak applied force, as seen in Fig. 4a. The reactive force from the artery is assessed based on the boundary velocity and pressure values at the inlet and outlet, respectively. The soft artery deforms more than it resists the pulsatile flow; hence, the reactive force derived from the fluid pressure variation is $39.4 \pm 2.3\mathrm{mN}$. Conversely, a rigid artery exhibits increased resistance to flow, yielding a higher force feedback of $128.6 \pm 2.2\mathrm{mN}$, as illustrated in Fig. 4b. The greatest force resulting from arterial palpation, considering various elastic moduli of the artery from $0\,\mathrm{MPa}$ to $2\,\mathrm{MPa}$, is $2.5\,\mathrm{N}$ as seen in Fig. 4d. Consequently, the design of the sensor must accommodate a force range of $3\,\mathrm{N}$ with a resolution of $10\,\mathrm{mN}$. Basic mathematical analysis conveys haptic information solely through the normal applied and reactive forces. The mathematical determination of forces related to wall motions induced by Rayleigh waves with pulsation [54]

IEEE Transactions on Haptics (ToH) paper, presented at ICRA 2026, Vienna, Austria. Cite as ToH paper.

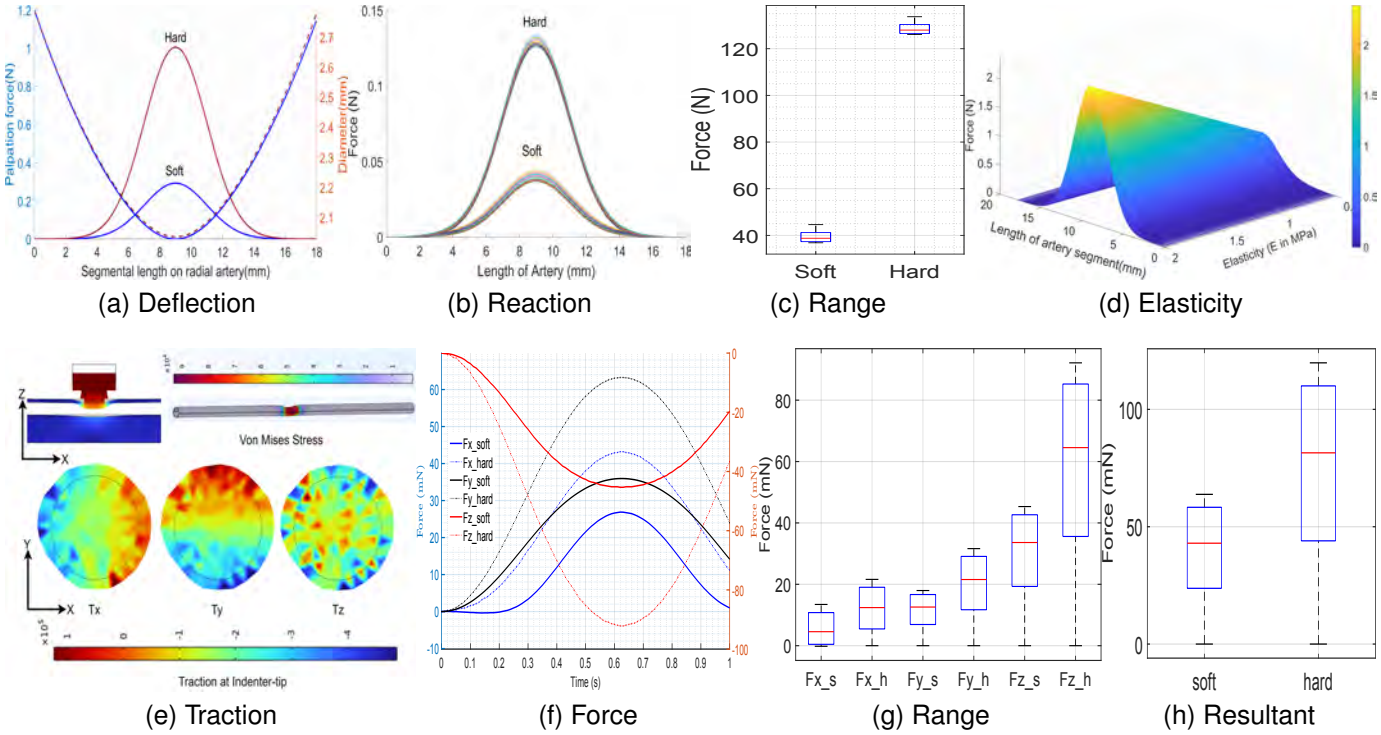

Fig. 4: **a**. The deflection of the soft and hard arteries by the Gaussian loads on top of the artery wherein the diameter reduces gradually from 2.79 mm to 2.02 mm at the center of the artery. **b**. The reactive force from the artery along the length of the palpated length for different boundary conditions as per 1c at 0.1, 0.2, 0.3, 0.4, 0.5, 0.6, 0.7, 0.8, 0.9 and 1s, **c.** The box plot of maximum reactive force for soft and hard arteries. **d.** The increase in force feedback with a rise in modulus elasticity of the artery.**e.** XZ-cross section of the artery while palpating through the indenter, showing the deformation and Von Misses stress of the artery at the palpation zone and the traction at the top surface of the indenter. **f.** The interactive force along X, Y, and Z axes for soft and hard arteries. **g.** The range of the forces depicted in the box plot. **h.** The range of resultant force for soft and hard arteries.

is complex; thus, they are investigated using simulation and experimental methods in the following sections IV-B, IV-D.

B. Force interaction in simulation

The artery exhibits an elliptical deformation upon palpation. Consequently, the contact surface of the indenter tip exhibits traction along the X, Y, and Z axes, as illustrated in Fig. 4e, Consequently, traction along the Z-axis refers to normal force, while traction along the X and Y axes refers to shear forces. The hard artery exhibits a higher force interaction along tri-axial directions compared to the soft artery in Fig. 4f, which accounts for the elevated pulse wave velocity (PWV) in rigid arteries [55]. The forces along the X, Y, and Z axes are 11.22 ± 10.13mN, 11.16 ± 6mN, and 29.24 ± 15.04mN for the soft artery, respectively, whereas they are 11.81 ± 7.42mN, 19.33 ± 10.51mN, and 57.2 ± 30.47mN for the hard artery, as shown in Fig. 4g. The magnitude of normal force interaction is higher than the shear force interaction. The range of resultant force interaction from the simulation is 42 ± 18mN and 81 ± 40mN for soft and hard arteries, respectively, within a single pulse, as shown in Fig. 4h. An elevated PWV is often associated with increased blood pressure [56]. A comparable effect is observed in hard artery palpation, where the force components along the X, Y, and Z axes surpass those of soft vasculature, as illustrated in Fig. 4g. The resultant force feedback obtained from simulation aligns closely with the analytical solution.

While the mathematical and simulation models treat vasculature as elastic and hyperelastic materials, respectively, real vascular tissue exhibits considerably more complex biomechanical behavior. To address this discrepancy, we conduct experimental analyses using the Subblescope [51] on synthetic soft and hard arteries, as well as on the radial artery of human participants, to obtain empirical measurements of force and deformation during palpation.

C. Force interaction from arteries during experiment

The pressure from the transducers in HEMA, connected to the mock vessel and at the end of the soft artery, records between 72.84 mmHg to 108.62 mmHg as shown in Fig. 5a. The phase delay between the two pulse waves is 25.4^0. The force interaction measured for the hard silicone artery exceeds that of the soft silicone artery along the radial (F_z), tangential (F_y), and longitudinal (F_x) directions. However, the variability of these forces is lower in the hard artery, as shown in Fig. 5d. The force along X, Y, Z for the soft artery is 48 ± 8 mN, 46 ± 14 mN, 390 ± 6 mN respectively. Similarly, the force interaction for hard artery is 81 ± 6 mN, 83 ± 5 mN, 496 ± 3 mN respectively. The force map for soft and hard arteries is constructed from the relative magnitudes of forces along the three axes from the sensor as shown in Fig. 5b, 5c. The force map has been plotted from the force data for 60 s during pulsatile flow by the HEMA. These spatial force distributions can potentially serve as diagnostic indicators for vascular pathologies.

IEEE Transactions on Haptics (ToH) paper, presented at ICRA 2026, Vienna, Austria. Cite as ToH paper.

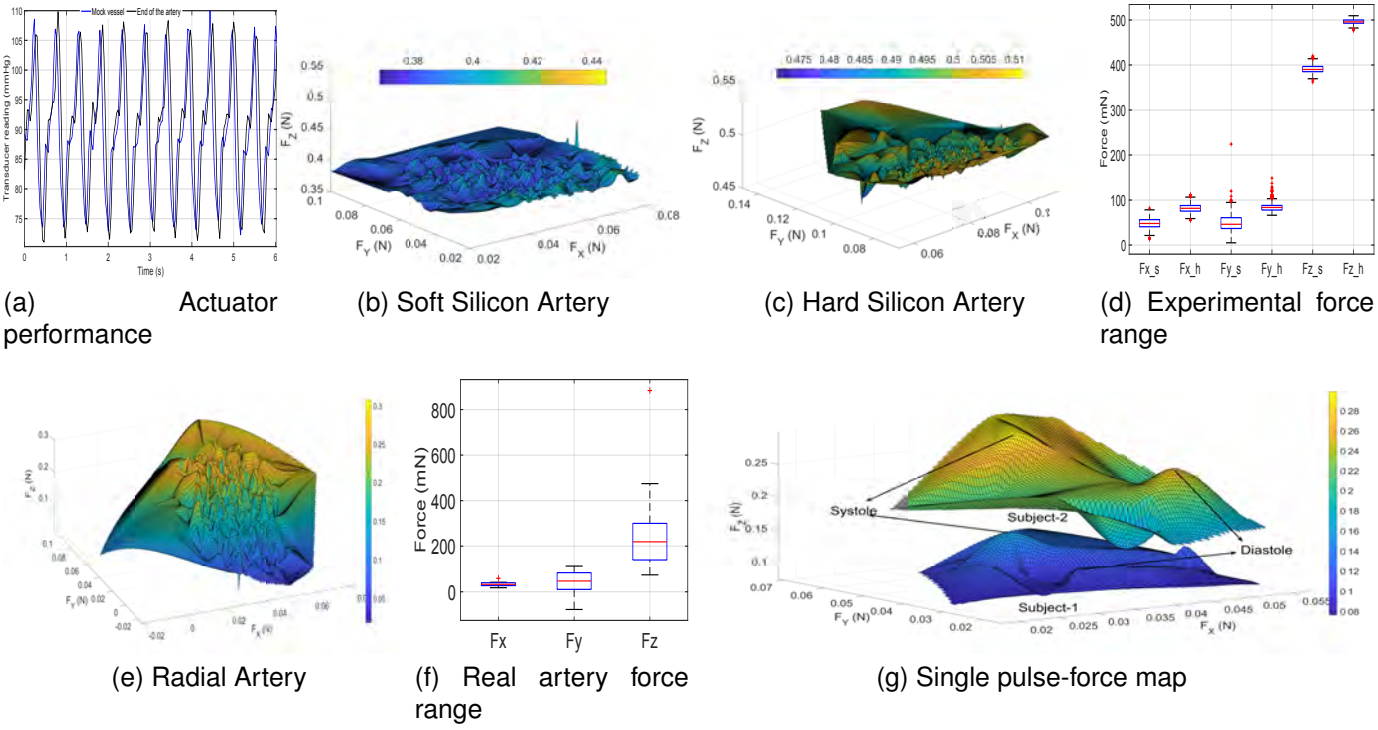

(a) Actuator performance (b) Soft Silicon Artery (c) Hard Silicon Artery (d) Experimental force range

(e) Radial Artery (f) Real artery force range (g) Single pulse-force map

Fig. 5: **a**. The pressure at the mock vessel (blue line) and end of the artery (black line) for the soft artery. The force map of **b.** soft and **c.** silicon arteries. **d.** The force ranges during the experiment from soft (Fx_s, Fy_s, Fz_s) and hard (Fx_h, Fy_h, Fz_h) arteries.**e**.Force map from the radial artery of a typical subject's pulse spanning for a minute. **f.** The range of F_x, F_y, F_z in the box plot from the radial artery of the participants. **g.** The force map of a single pulse of two typical subjects, wherein subject-2 has the higher arterial hardness.

The force interaction measured experimentally using HEMA is higher than that predicted by theoretical models. This discrepancy is primarily due to force dissipation through the hypodermis in simulations and the exclusion of inertial effects in the mathematical model. Additionally, in the experimental setup, the indenter is in direct contact with the artery, with no intermediate tissue layer, enabling direct observation of shear components arising from fluid-structure interaction. Attempts to replicate this configuration in simulation result in non-convergent solutions due to inconsistent contact between the cylindrical indenter and the circular artery. This issue is further examined in the subsequent section on force recording from the radial artery in human participants.

D. Force interaction from real arteries

The forces from the artery transmit through connective tissue around it before reaching the indenter tip of the sensor. The thickness of the connective tissue varies across the subjects and hence the transmitted force. The force map of a typical subject has been shown in Fig. 5e. The average force values for 60 s of the participants are used for getting the force ranges. The force ranges are 32.0 ± 6.0 mN, 47.0 ± 37.0 mN, and 219.0 ± 100.0 mN along the X, Y, and Z axes, respectively, as shown in Fig. 5f. The variability of longitudinal, transverse, and radial forces (normal force) is in increasing order, depicting higher arterial oscillations along normal directions than the tangential directions. The force map of a single pulse of two participants having ages 25 and 35 years has been shown in Fig. 5g, depicting the effect of age-related stiffening of the artery with a significantly ($p < 0.05$) higher systolic and diastolic force. Furthermore, the force distribution is not symmetric, and such a map may introduce components of pulse wave velocity, not only along the longitudinal direction but also along a transverse direction, which has not been explored in the literature.

V. Discussion

The haptics of pulse palpation are governed by the interaction between the externally applied force and the internal blood flow dynamics within the arteries. This interaction induces radial, axial, and tangential stresses, as well as arterial wall motion, resulting from intraluminal pressure and wall shear stress [57], [58]. The magnitude of the perceived force is also influenced by the external palpation force at which the intravascular pressure reaches its peak, corresponding to the most distinguishable point on the pressure-strength curve [59].

Additionally, artery palpation enhances the complexity of force interaction due to the pulsatile flow through a converging-diverging elliptical channel, introducing geometric non-uniformity and asymmetry. The wall shear stress and its spatial asymmetry increase with the degree of ellipticity (ϵ) [60], and they vary with angular position along the arterial wall. This variation has the potential to produce distinctive spatial force maps, offering valuable physiological insights and potential diagnostic markers.

The force and deformation are complementary to each other, and at an instance, either the force or the deformation

IEEE Transactions on Haptics (ToH) paper, presented at ICRA 2026, Vienna, Austria. Cite as ToH paper.

TABLE I: A comparison between reactive force (mN) from the palpated artery in literature and this study

Metrics	Physiological Significance	Literature	Analytical	Simulation	Experiment	Real artery
F_z (mN)	blood pressure, heart rate, vascular tone, wall thickness, arterial stiffness [12]	45.5 to 409.53 [61]	37.3 to 130.36	19.3 to 85.25	385.18 to 500.0	139.2 to 300.0
F_y (mN)	Endothelium dysfunction, permeability, lipo protein accumulation [65]	20 to 60 [57]	-	6.9 to 29.09	36.78 to 88.01	13.54 to 86.41
F_x (mN)	Shear force from axial blood, and wall stress [63] depends on their constituents, shear dependent thrombsis [66].	32.7 to 81.7 [64]	-	5.46 to 19.03	40.64 to 87.85	26.06 to 39.75

can be recorded. The normal force interaction depends on the blood pressure of the fluid. During robotic indentation at three consecutive locations on the radial artery, there is a pressure distribution varying from 0.02 to 0.18 psi [61] during pulsation, which corresponds to a normal pulse force (F_z) of $45.5\,\mathrm{mN}$ to $409.53\,\mathrm{mN}$, assuming a contact area of the fingertip as $0.000\,33\,\mathrm{m}^2$ [62]. The axial force (F_x) arises due to axial stretch, which is essential to maintain the structural and functional integrity of the artery during blood flow [63]. The axial force is the summation of the force due to axial stretch and wall shear stress (WSS). For a passive artery with a radius of $1.3\,\mathrm{mm}$ and a stretch in the range of 1.5 to 1.8, the resulting axial force ranges from $20\,\mathrm{mN}$ to $60\,\mathrm{mN}$ [57]. The wall shear stress (WSS) during artery constriction varies between -30 to 120.0 $dyne/cm^2$ [58]. Consequently, the axial force due to WSS varies between $-1\,\mathrm{mN}$ to $4\,\mathrm{mN}$.

The transverse force depends on the circumferential stress (σ_θ). The incremental σ_θ in the artery varies between $8\,\mathrm{kPa}$ to $20\,\mathrm{kPa}$ across the aspect ratio ($\frac{a}{b}, a, b =$ major, minor-lengths) of 1 to 3 [64], which corresponds to a force of $32.7\,\mathrm{mN}$ to $81.7\,\mathrm{mN}$ for the radial artery. The significance of these force components is discussed in Table I, which includes a comparative analysis of the palpation-force metrics between the literature and this study. The force ranges presented in the table are derived from the interquartile range (IQR) of the data. The forces evaluated both theoretically and experimentally fall within the range of forces reported in the literature and are predominantly greater than the just-noticeable difference (JND) of the fingertips. Most existing studies focus primarily on the theoretical analysis of stress developed in the artery due to blood flow, particularly under pathological conditions. However, there is limited literature addressing the comprehensive force interactions exerted by arteries in directions other than the radial direction.

A. Clinical Significance

Forces arising from arterial wall motion have significant clinical implications for cardiovascular diseases (CVDs) and vascular disorders [67]. These forces are intrinsically linked to cardiovascular dynamics; therefore, any physiological alteration can modify the force vectors within the artery. The haptic perception involved in pulse palpation depends on the sensitivity thresholds of physicians' fingertips. Specifically, the radial and circumferential forces in the artery correlate with parameters such as blood pressure, intima-media thickness (IMT), and arterial wall stiffness, often quantified by pulse wave velocity (PWV). Additionally, wall shear stress (WSS) has been associated with conditions including diabetes, kidney disease, atherosclerosis, endothelial permeability, and stenosis [68]. Recent advancements in prosthetic fingertip sensors have resulted in enhanced force sensitivity surpassing that of the human fingertip [69]. However, these sensors tend to saturate under applied forces, which limits their ability to detect reaction forces from the pulse with high precision and resolution at the millinewton scale. Consequently, the development of sensors capable of bidirectional force sensing is essential for generating accurate force maps across various arterial structures.

B. Limitations and future work

This research aims to quantify haptic cues in terms of three-dimensional force interactions during pulse palpation to support the development of sensor and actuation systems for physician training. The magnitude of force feedback obtained from simulations is relatively higher than that observed in vivo, as the sensor maintains direct contact with the artery, enabling more efficient force transmission with minimal dissipation. In the mathematical analysis, only the palpated segment of the artery is considered, since including the entire arterial length would unnecessarily complicate the model without significantly affecting the results. The outcomes of the mathematical analysis correspond closely with experimental findings. It is important to note that the mathematical model does not account for deformation of the artery's bottom layer during palpation. In practical scenarios, when the fluid is confined, it exerts force on the bottom layer of the artery, inducing bending. This bending effect has been examined in both the simulation model and experimental investigations. The experimental setup may be enhanced by incorporating an anemometer to measure fluid velocity. The hydro-electromagnetic actuator (HEMA) employed produces precise force feedback comparable to that generated by human arteries. Therefore, fluid-based haptic actuators demonstrate advantages over alternative actuation methods for pulse palpation applications. The magnitude of force generated by HEMA at varying plunger velocities has yet to be fully evaluated. A comprehensive characterization of the actuator's capacity to reproduce diverse pulse profiles for training purposes will be undertaken in future work.

VI. Conclusion

The fingertip perceives not only normal force feedback but also shear force feedback along the transverse and longitudinal axes during palpation. The overall magnitude of force increases with arterial stiffness; however, the variability in force (represented by the area of the force map) decreases.

IEEE Transactions on Haptics (ToH) paper, presented at ICRA 2026, Vienna, Austria. Cite as ToH paper.

Therefore, effective pulse actuators must incorporate both normal and shear force feedback to accurately simulate the pulse, necessitating the use of fluid-based actuation systems. In this study, the hydro-electromagnetic actuator successfully generates the tactile patterns of pulse palpation observed using the Subblescope. The sensor-actuator system developed for pulse palpation training and remote diagnosis depends on precise detection and delivery of haptic feedback. This haptic information includes both tactile and kinesthetic components. The kinesthetic feedback facilitates prehensile movements of the artery, while the tactile feedback encompasses dynamics of the artery in synchrony with the pulse. The Subblescope effectively detects both normal and shear forces from the pulse in synthetic arteries and radial arteries of participants. Further research is necessary to investigate the shear and normal force components under turbulent, non-Newtonian blood flow conditions. Additional testing and iterative refinement are required to validate the effectiveness of the haptic sensor-actuator system under pathological conditions.

ACKNOWLEDGMENTS

I would like to express my gratitude to my lab colleagues for their suggestions.

REFERENCES

[1] J. R. Napier, "The prehensile movements of the human hand," *The Journal of bone and joint surgery. British volume*, vol. 38, no. 4, pp. 902–913, 1956.

[2] H. T. Marx and N. Y. Paul, "Clinical examination of the arterial pulse," *Progress in Cardiovascular Diseases*, vol. 10, no. 3, pp. 207–235, 1967.

[3] M. A. Bailey, K. J. Griffin, and D. J. A. Scott, "Clinical assessment of patients with peripheral arterial disease," in *Seminars in interventional radiology*, vol. 31, no. 04. Thieme Medical Publishers, 2014, pp. 292–299.

[4] M. E. Alnaeb, N. Alobaid, A. M. Seifalian, D. P. Mikhailidis, and G. Hamilton, "Optical techniques in the assessment of peripheral arterial disease," *Current vascular pharmacology*, vol. 5, no. 1, pp. 53–59, 2007.

[5] R. B. Gowda, P. Sharan, K. Saara, M. Braim, and A. N. Alodhayb, "An fbg-based optical pressure sensor for the measurement of radial artery pulse pressure," *Journal of Biophotonics*, vol. 17, no. 7, p. e202400083, 2024.

[6] D. Lin, A. Zhang, J. Gu, X. Chen, Q. Wang, L. Yang, Y. Chou, G. Liu, and J. Wang, "Detection of multipoint pulse waves and dynamic 3d pulse shape of the radial artery based on binocular vision theory," *Computer Methods and Programs in Biomedicine*, vol. 155, pp. 61–73, 2018.

[7] Y. Rong, K. V. Mishra, and D. W. Bliss, "Radar-based radial arterial pulse rate and pulse pressure analysis," in *2021 29th European Signal Processing Conference (EUSIPCO)*. IEEE, 2021, pp. 1870–1874.

[8] S. Toohey, A. Wray, J. Hunter, I. Waldrop, S. Saadat, M. Boysen-Osborn, G. Sudario, J. Smart, W. Wiechmann, S. D. Pressman *et al.*, "Comparing the psychological effects of manikin-based and augmented reality–based simulation training: Within-subjects crossover study," *JMIR Medical Education*, vol. 8, no. 3, p. e36447, 2022.

[9] N. D. Chandrashekar, S. Safford, M. Muniyandi, and D. Gračanin, "An extended reality simulator for pulse palpation training," in *2023 IEEE Conference on Virtual Reality and 3D User Interfaces Abstracts and Workshops (VRW)*. IEEE, 2023, pp. 178–182.

[10] T. R. Coles, N. W. John, D. Gould, and D. G. Caldwell, "Integrating haptics with augmented reality in a femoral palpation and needle insertion training simulation," *IEEE transactions on haptics*, vol. 4, no. 3, pp. 199–209, 2011.

[11] H. Luo, Y. Fu, N. Ding, C. Dong, Y. Zhang, and D. Wang, "Hap-pulse: A wearable vibrotactile glove for medical pulse wave rendering," *IEEE Transactions on Haptics*, vol. 15, no. 2, pp. 280–291, 2022.

[12] C. E. Athaide, B. Spronck, and J. S. Au, "Physiological basis for longitudinal motion of the arterial wall," *American Journal of Physiology-Heart and Circulatory Physiology*, vol. 322, no. 5, pp. H689–H701, 2022.

[13] S. Salles, A. J. Chee, D. Garcia, C. Alfred, D. Vray, and H. Liebgott, "2-d arterial wall motion imaging using ultrafast ultrasound and transverse oscillations," *IEEE Transactions on Ultrasonics, Ferroelectrics, and Frequency Control*, vol. 62, no. 6, pp. 1047–1058, 2015.

[14] C. Hatzfeld, S. Cao, M. Kupnik, and R. Werthschützky, "Vibrotactile force perception–absolute and differential thresholds and external influences," *IEEE transactions on haptics*, vol. 9, no. 4, pp. 586–597, 2016.

[15] J. M. Thornbury and C. M. Mistretta, "Tactile sensitivity as a function of age," *Journal of gerontology*, vol. 36, no. 1, pp. 34–39, 1981.

[16] G. N. K. Reddy, M. S. Manikandan, and N. N. Murty, "Performance of spectral, autocorrelation and peak count based pr estimation methods under normal/abnormal ppg for wearable devices," in *2021 IEEE International Conference on Health, Instrumentation & Measurement, and Natural Sciences (InHeNce)*. IEEE, 2021, pp. 1–6.

[17] C. Yamahata, C. Lotto, E. Al-Assaf, and M. Gijs, "A pmma valveless micropump using electromagnetic actuation," *Microfluidics and Nanofluidics*, vol. 1, pp. 197–207, 2005.

[18] J. Judy, T. Tamagawa, and D. Polla, "Surface micromachined linear thermal microactuator," in *International Technical Digest on Electron Devices*. IEEE, 1990, pp. 629–632.

[19] W. Qiu, J. Zhong, T. Jiang, Z. Li, M. Yao, Z. Shao, Q. Cheng, J. Liang, D. Wang, Y. Peng *et al.*, "A low voltage-powered soft electromechanical stimulation patch for haptics feedback in human-machine interfaces," *Biosensors and Bioelectronics*, vol. 193, p. 113616, 2021.

[20] K. A. Li, P. Baudisch, W. G. Griswold, and J. D. Hollan, "Tapping and rubbing: exploring new dimensions of tactile feedback with voice coil motors," in *Proceedings of the 21st annual ACM symposium on User interface software and technology*, 2008, pp. 181–190.

[21] K. Junwu, Y. Zhigang, P. Taijiang, C. Guangming, and W. Boda, "Design and test of a high-performance piezoelectric micropump for drug delivery," *Sensors and Actuators A: Physical*, vol. 121, no. 1, pp. 156–161, 2005.

[22] C. P. Premarathna, D. S. Chathuranga, and T. D. Lalitharatne, "Fabrication of a soft tactile display based on pneumatic balloon actuators and voice coils: Evaluation of force and vibration sensations," in *2017 IEEE/SICE International Symposium on System Integration (SII)*. IEEE, 2017, pp. 763–768.

[23] O. C. Jeong and S. S. Yang, "Fabrication and test of a thermopneumatic micropump with a corrugated p+ diaphragm," *Sensors and Actuators A: Physical*, vol. 83, no. 1-3, pp. 249–255, 2000.

[24] W. Benard, H. Kahn, A. Heuer, and M. Huff, "A titanium-nickel shape-memory alloy actuated micropump," in *Proceedings of International Solid State Sensors and Actuators Conference (Transducers' 97)*, vol. 1. IEEE, 1997, pp. 361–364.

[25] J.-H. Koo, T. Tantiyartyanontha, Y.-M. Kim, H. Kang, and T.-H. Yang, "Application of magneto-rheological fluids for generating a wide range of radial pulse waveforms," *Smart Materials and Structures*, vol. 27, no. 12, p. 125010, 2018.

[26] M. Eaton, J.-H. Koo, T.-H. Yang, and Y.-M. Kim, "Replication of radial pulses using magneto-rheological fluids," *Micromachines*, vol. 15, no. 8, p. 1010, 2024.

[27] T.-H. Yang, J. U. Kim, Y.-M. Kim, J.-H. Koo, and S.-Y. Woo, "A new blood pulsation simulator platform incorporating cardiovascular physiology for evaluating radial pulse waveform," *Journal of healthcare engineering*, vol. 2019, no. 1, p. 4938063, 2019.

[28] H. Liu, D. Yan, Q. Deng, J. Lin, and W. Sun, "A design of pulse condition simulation device based on squeeze mode," in *4th International Conference on Information Technology and Management Innovation*. Atlantis Press, 2015, pp. 240–246.

[29] T.-H. Yang, J.-I. Kim, J.-H. Koo, G. Jo, and Y.-M. Kim, "Advancing radial arterial pulsation simulation: Wave decomposition modeling with hardware implementation," *IEEE Access*, 2024.

[30] M. Kandee, P. Boonbrahm, and S. Boonbrahm, "Realistic pulse simulation measurement using haptic device with augmented reality," in *IECON 2016-42nd Annual Conference of the IEEE Industrial Electronics Society*. IEEE, 2016, pp. 773–778.

[31] P.-J. Lu, M.-Y. Chan, S. Tsui, T.-T. Shen, and J.-C. Chang, "Development of an anatomy-mimicking, wave transport-preserving mock circulation loop for evaluating pulsatile hemodynamics as supported by cardiovascular assist devices," *Cardiovascular Engineering and Technology*, pp. 1–20, 2025.

[32] F. Bardi, E. Gasparotti, E. Vignali, S. Avril, and S. Celi, "A hybrid mock circulatory loop for fluid dynamic characterization of 3d anatomical phantoms," *IEEE Transactions on Biomedical Engineering*, vol. 70, no. 5, pp. 1651–1661, 2022.

IEEE Transactions on Haptics (ToH) paper, presented at ICRA 2026, Vienna, Austria. Cite as ToH paper.

[33] C. E. Taylor and G. E. Miller, "Mock circulatory loop compliance chamber employing a novel real-time control process," *Journal of medical devices*, vol. 6, no. 4, p. 045003, 2012.

[34] E. Cuenca-Navalon, T. Finocchiaro, M. Laumen, A. Fritschi, T. Schmitz-Rode, and U. Steinseifer, "Design and evaluation of a hybrid mock circulatory loop for total artificial heart testing," *The International journal of artificial organs*, vol. 37, no. 1, pp. 71–80, 2014.

[35] F. Cappon, T. Wu, T. Papaioannou, X. Du, P.-L. Hsu, and A. W. Khir, "Mock circulatory loops used for testing cardiac assist devices: A review of computational and experimental models," *The International Journal of Artificial Organs*, vol. 44, no. 11, pp. 793–806, 2021.

[36] W. Hong, "A mock circulation loop for in vitro hemodynamics in human arterial systems with applications," Ph.D. dissertation, Purdue University Graduate School, 2025.

[37] A. H. Shapiro, "Steady flow in collapsible tubes," 1977.

[38] V. Vavourakis, Y. Papaharilaou, and J. Ekaterinaris, "Coupled fluid–structure interaction hemodynamics in a zero-pressure state corrected arterial geometry," *Journal of biomechanics*, vol. 44, no. 13, pp. 2453–2460, 2011.

[39] K. Agarwal and D. Chatterjee, "The role of encapsulated microbubbles in the diagnosis of stenosis in arteries," in *Journal of Physics: Conference Series*, vol. 656, no. 1. IOP Publishing, 2015, p. 012002.

[40] N. S. Kelly, H. S. Gill, A. N. Cookson, and K. H. Fraser, "Influence of shear-thinning blood rheology on the laminar-turbulent transition over a backward facing step," *Fluids*, vol. 5, no. 2, p. 57, 2020.

[41] D. Getachew, A. Astatkie, and K. Lemma, "Diameter, vessel thickness and angle of bifurcation of the radial artery in ethiopian cadavers," *Journal of Morphological Sciences*, vol. 35, no. 02, pp. 129–135, 2018.

[42] T. Khamdaeng, J. Luo, J. Vappou, P. Terdtoon, and E. Konofagou, "Arterial stiffness identification of the human carotid artery using the stress–strain relationship in vivo," *Ultrasonics*, vol. 52, no. 3, pp. 402–411, 2012.

[43] K. Dandekar, B. I. Raju, and M. A. Srinivasan, "3-d finite-element models of human and monkey fingertips to investigate the mechanics of tactile sense," *J. Biomech. Eng.*, vol. 125, no. 5, pp. 682–691, 2003.

[44] S. Saeid Khalafvand and H.-C. Han, "Stability of carotid artery under steady-state and pulsatile blood flow: A fluid–structure interaction study," *Journal of Biomechanical Engineering*, vol. 137, no. 6, 2015.

[45] B. B. Lieber, "Arterial macrocirculatory hemodynamics," *The biomedical engineering handbook*, vol. 1, 2000.

[46] M. Sharzehee, S. S. Khalafvand, and H.-C. Han, "Fluid-structure interaction modeling of aneurysmal arteries under steady-state and pulsatile blood flow: a stability analysis," *Computer methods in biomechanics and biomedical engineering*, vol. 21, no. 3, pp. 219–231, 2018.

[47] L. H. Peterson, R. E. Jensen, and J. Parnell, "Mechanical properties of arteries in vivo," *Circulation Research*, vol. 8, no. 3, pp. 622–639, 1960.

[48] L. R. Treloar, "The mechanics of rubber elasticity," *Proceedings of the Royal Society of London. A. Mathematical and Physical Sciences*, vol. 351, no. 1666, pp. 301–330, 1976.

[49] J. Z. Wu, D. E. Welcome, T. W. McDowell, X. S. Xu, and R. G. Dong, "Modeling of the interaction between grip force and vibration transmissibility of a finger," *Medical engineering & physics*, vol. 45, pp. 61–70, 2017.

[50] R. Mahdavi, S. Hashemi-Najafabadi, M. A. Ghiass, and C. B. Adiels, "Microfluidic design for in-vitro liver zonation—a numerical analysis using comsol multiphysics," *Medical & biological engineering & computing*, vol. 62, no. 1, pp. 121–133, 2024.

[51] D. Subudhi, P. K. Routray, and M. Muniyandi, "Subblescope: Novel thin film haptic sensing using a single bubble approach," *IEEE Sensors Journal*, 2024.

[52] I. Ozolanta, G. Tetere, B. Purinya, and V. Kasyanov, "Changes in the mechanical properties, biochemical contents and wall structure of the human coronary arteries with age and sex," *Medical engineering & physics*, vol. 20, no. 7, pp. 523–533, 1998.

[53] H. Tanaka, K. D. Monahan, and D. R. Seals, "Age-predicted maximal heart rate revisited," *Journal of the american college of cardiology*, vol. 37, no. 1, pp. 153–156, 2001.

[54] Z. I. Dimitrova and N. K. Vitanov, "Travelling waves connected to blood flow and motion of arterial walls," in *Water in Biomechanical and Related Systems*. Springer, 2021, pp. 243–263.

[55] P. Nabeel, V. R. Kiran, J. Joseph, V. Abhidev, and M. Sivaprakasam, "Local pulse wave velocity: theory, methods, advancements, and clinical applications," *IEEE Reviews in Biomedical Engineering*, vol. 13, pp. 74–112, 2019.

[56] Y. Ma, J. Choi, A. Hourlier-Fargette, Y. Xue, H. U. Chung, J. Y. Lee, X. Wang, Z. Xie, D. Kang, H. Wang *et al.*, "Relation between blood pressure and pulse wave velocity for human arteries," *Proceedings of the National Academy of Sciences*, vol. 115, no. 44, pp. 11 144–11 149, 2018.

[57] G. A. Holzapfel and R. W. Ogden, "Constitutive modelling of arteries," *Proceedings of the Royal Society A: Mathematical, Physical and Engineering Sciences*, vol. 466, no. 2118, pp. 1551–1597, 2010.

[58] V. Deplano and M. Siouffi, "Experimental and numerical study of pulsatile flows through stenosis:: Wall shear stress analysis," *Journal of biomechanics*, vol. 32, no. 10, pp. 1081–1090, 1999.

[59] G. Wang, X. Geng, X. Kang, Y. Zhang, J. Zhang, and H. Zhang, "A novel radial artery ps curve model based on radial vibration of vascular wall," *Applied Sciences*, vol. 12, no. 19, p. 9706, 2022.

[60] M. B. Robertson, U. Köhler, P. R. Hoskins, and I. Marshall, "Flow in elliptical vessels calculated for a physiological waveform," *Journal of vascular research*, vol. 38, no. 1, pp. 73–82, 2001.

[61] K. W. Kong, W.-M. Lau, K. S. Wong, H.-Y. Chan, F. C. S. Lee, J. Shen, V. T. C. W. Wong, and W. J. Li, "A pulse-sensing robotic hand for tactile arterial palpation," in *2016 IEEE International Conference on Cyber Technology in Automation, Control, and Intelligent Systems (CYBER)*. IEEE, 2016, pp. 141–145.

[62] V. S. Morash, A. E. C. Pensky, and J. A. Miele, "Effects of using multiple hands and fingers on haptic performance," *Perception*, vol. 42, no. 7, pp. 759–777, 2013.

[63] J. Humphrey, J. Eberth, W. Dye, and R. Gleason, "Fundamental role of axial stress in compensatory adaptations by arteries," *Journal of biomechanics*, vol. 42, no. 1, pp. 1–8, 2009.

[64] Y. Shoji, S. Mori, M. Arakawa, S. Ohba, K. Kobayashi, and H. Kanai, "Accurate measurement of elasticity of the radial artery wall considering changes in cross-sectional shape of artery caused by pushing pressure applied by ultrasound probe," *Japanese Journal of Applied Physics*, vol. 61, no. SG, p. SG1043, 2022.

[65] M. A. Gimbrone Jr, K. R. Anderson, and J. N. Topper, "The critical role of mechanical forces in blood vessel development, physiology and pathology," *Journal of vascular surgery*, vol. 29, no. 6, pp. 1104–1151, 1999.

[66] D. N. Ku, "Blood flow in arteries," *Annual review of fluid mechanics*, vol. 29, no. 1, pp. 399–434, 1997.

[67] D. Wang, L. Vahala, and Z. Hao, "Radial and longitudinal motion of the arterial wall: Their relation to pulsatile pressure and flow in the artery," *Physical Review E*, vol. 98, no. 3, p. 032402, 2018.

[68] J. Malik, L. Novakova, A. Valerianova, E. Chytilova, V. Lejsek, K. Buryskova Salajova, L. Lambert, T. Grus, M. Porizka, and P. Michalek, "Wall shear stress alteration: a local risk factor of atherosclerosis," *Curr Atheroscler Rep*, vol. 24, no. 3, pp. 143–151, 2022.

[69] N. Dvorak, K. Chung, K. Mueller, and P.-C. Ku, "Ultrathin tactile sensors with directional sensitivity and a high spatial resolution," *Nano Letters*, vol. 21, no. 19, pp. 8304–8310, 2021.

Debadutta Subudhi Debadutta Subudhi received his bachelor's degree in Mechanical Engineering and M.S. from the Indian Institute of Technology Madras. He is currently pursuing his doctoral degree at the Indian Institute of Technology Madras, located in Chennai, India.

K K Deepak Prof. K. K. Deepak (MBBS, MD, PhD, and DSc) is currently a Visiting Professor at the Centre for Biomedical Engineering, IIT Delhi, and an adjunct Professor at IIT Madras. He set up the first Autonomic Function Lab in 1989 and the first Vascular Function Lab in 2000 in India for research, technological developments, education, and clinical services. He established the Space Physiology lab at AIIMS (2013).

Manivannan M. Muniyandi Manivannan received the M.E. and Ph.D. degrees from the Indian Institute of Science, Bangalore, India. He received postdoctoral training in Haptics at the Massachusetts Institute of Technology (MIT), Cambridge, MA, USA. Before MIT, he received other 'postdoctoral training in CAD standards and sensor networks at the National Institute of Standards and Technology, Gaithersburg, MD, USA. He is currently with the Indian Institute of Technology Madras, Chennai, India.